

Ames Research Center
11-02-CR

JOINT INSTITUTE FOR AERONAUTICS AND ACOUSTICS

51150

P-38



National Aeronautics and
Space Administration

Ames Research Center

JIAA TR - 104

Stanford University

Computational Study of the Aerodynamics and Control by Blowing of Asymmetric Vortical Flows over Delta Wings

By

Ken Craig

Stanford University
Department of Aeronautics and Astronautics
Stanford, CA 94305

September 1991

(NASA-CR-187979) COMPUTATIONAL STUDY OF THE
AERODYNAMICS AND CONTROL BY BLOWING OF
ASYMMETRIC VORTICAL FLOWS OVER DELTA WINGS
(Stanford Univ.) 38 p CSCL 01A

N92-10990

Unclas
G3/02 0051150

Vertical text on the left edge of the page.

Vertical text on the right edge of the page.

Abstract

This report describes some of the work done in a study of the flowfield produced by tangential leading-edge blowing on a 60-degree delta wing. The flow is investigated computationally by solving the Thin-Layer Navier-Stokes equations. Steady-state flowfields are calculated for various angles of attack and yaw, with and without the presence of tangential leading-edge blowing. The effectiveness of blowing as a rolling moment control mechanism to extend the envelope of controllability is illustrated at pre- and post-stall angles of attack. The numerical grid is generated using algebraic grid generation and various interpolation and blending techniques. The jet emanates from a slot with linearly-varying thickness and is introduced into the flowfield using the concept of an actuator plane, thereby not requiring resolution of the jet slot geometry. The Baldwin-Lomax algebraic turbulence model is used to provide turbulent closure. The computational results are compared with those of experiments.

Table of Contents

Abstract.....	2
Nomenclature.....	4
1. Introduction.....	5
2. Geometry.....	6
3. Grid Generation.....	7
3.1 Topology.....	7
3.2 Orthogonality.....	8
3.3 Zonal arrangement.....	9
4. Numerical method.....	9
5. Actuator plane concept.....	10
6. Results and Discussion.....	10
6.1 No blowing cases.....	11
6.1.1 $\alpha=30^\circ$, $\beta=0^\circ$	11
6.1.2 $\alpha=50^\circ$, $\beta=0^\circ$	12
6.1.3 $\alpha=30^\circ$, $\beta=10^\circ$	12
6.1.4 $\alpha=50^\circ$, $\beta=10^\circ$	13
6.2 Blowing cases.....	13
6.2.1 $\alpha = 30^\circ$, $\beta = 0^\circ$	13
6.3 Comparison with experiment.....	15
6.3.1 Comparison of pressure coefficients.....	15
6.3.2 Comparison of rolling moment coefficient.....	16
6.3.3 Comparison of normal force coefficient.....	16
6.3.4 Comparison of pitching moment coefficient.....	17
7. Future work.....	18
8. Conclusions.....	19
9. Acknowledgements.....	19
References.....	20

Nomenclature

C_L	wing lift coefficient
C_N	wing normal force coefficient
C_{Mx}	wing rolling moment coefficient
C_{My}	wing pitching moment coefficient
C_μ	blowing momentum coefficient
α	angle of attack
β	yaw angle
M_∞	freestream Mach number
S_{ref}	wing reference area
Re	Reynolds number based on wing chord
U_j	jet velocity
\dot{m}_j	jet mass flow rate
q_∞	dynamic pressure
AR	aspect ratio
$C_{p_{stag}}$	stagnation pressure coefficient

1. Introduction

The extension of the high angle of attack (α) regime of delta wing aircraft has been of considerable interest in recent years. It is well known that the flow at high α over delta wings is dominated by two leading-edge vortices. Previous studies have shown the occurrence of vortex asymmetry and burst, the first of which leads to the wing rock phenomenon. Both vortex asymmetry and burst cause non-linear and often unpredictable aerodynamic forces and moments. Since conventional control surfaces are ineffective at high α , it is desirable to have a mechanism which would control the strength and location of these leading-edge vortices.

By modifying the vortical flowfield, tangential leading-edge blowing (TLEB) has been shown experimentally and computationally to be a viable option in providing roll control for delta wings at high α as in Refs. 1 and 2. These studies were for a half-span wing assuming symmetry. More recently, experimental studies were performed using a full-span wing.^{3,4} The effectiveness of TLEB was again demonstrated but there is coupling between the blown and unblown sides for pre-stall angles of attack. Data from these studies include force and moment coefficients as well as surface pressures and laser sheet flow visualization at one downstream station.

Previous computational studies of the subsonic flow over delta wings at high alpha have mainly concentrated on wings with sharp leading edges¹⁰⁻¹⁶ where separation is generally fixed. A round leading edge necessitates the use of a viscous method in order to determine the exact location of the primary separation line. The accuracy of the location of the separation line plays an important role in the

trajectory of the leading-edge vortex, and therefore on the aerodynamics of the flow.

The current report describes part of a computational study solving the thin-layer form of the Navier-Stokes equations for the flow about the same full-span model as used in the aforementioned experiments.^{3,4} The numerical grid is generated algebraically using various blending and interpolation functions. The jet slot is not modelled explicitly in the grid (as by Yeh et al² for a half-span delta wing), but is introduced using the actuator plane concept as used by Tavella et al⁵ and Font et al.⁶ The flow is solved using the F3D code, which has been successfully applied to high α flow.^{5,6,7} The Baldwin-Lomax half-equation algebraic turbulence model,⁸ with modifications suggested by Degani and Schiff,⁹ is used to provide turbulent closure.

The objectives of this study are:

- (i) to validate the current approach by comparing computational results with that of experiment,
- (ii) to provide a detailed description of the flowfield and aerodynamics governing the flow at angle of attack with and without the presence of blowing, and
- (iii) to show the effectiveness of TLEB as a roll control mechanism at high angles of attack.

2. Geometry

The delta wing used for this numerical experiment has a leading-edge sweep angle of 60° and is given in Fig. 1. The geometry is the same as that used for the experiments reported by Celik et al³ and Wood et al.⁴ The leading edges are round and the top and bottom surfaces of the wing are parallel with a constant thickness (6% at the root chord). The nose of the wing is generated by continuing the leading

edges to the apex. The result of this is a sharp nose when viewed from above but an elliptically shaped nose when viewed from the side. The wing is cropped to form a constant span tail or flap which is angled on the lower surface. The jet slots for blowing are situated on the wing leading edges from the nose-body junction to just short of the beginning of the wing tail.

3. Grid Generation

Due to the relatively simple grid topology required for this geometry, the grid about the delta wing is generated algebraically. Algebraic grid generation is efficient and therefore lends itself to grid refinement studies. The grid is generated in 2-D sections and then stacked together. Several post-processing steps are then performed, mainly through interpolation, to redistribute points in a desirable 3-D fashion. Vinokur¹⁷ stretching is used in the redistribution.

3.1 Topology

The grid topology is C-0. There are three sections to the original grid. The first is the nose which has a spherical cap. The generation of this cap is done in 2-D semi-circular disks which are stacked in the circumferential direction. The second section is the body of the wing where 2-D downstream cross-sections or cross-flow planes are generated. In cross-section the leading edge is elliptical since it is circular normal to the leading edge. The last section is the tail-wake region where 2-D downstream sections are again generated. Cross-sections of the tail are rectangular due to the cropped wing. A zero-thickness wake with flow-through conditions is added to the wing to allow for closure of the computational domain.

Stretching is employed in the downstream direction on the wing body and in the wake. The grid extends six chord lengths in front and nine chord lengths behind the wing.

3.2 Orthogonality

As suggested by Tavella,¹⁸ an algebraic grid can be improved by post-processing, particularly by blending onto desired functions close to a body surface. This is implemented by projecting the arc lengths of the existing grid at a surface onto a normal to the surface, and then blending the existing grid and the normal by using an inverse tangent function combination. The number of intervals blended, the grid location where the two functions being blended coincide (transition index), and the power of the blending functions need to be specified. The blending function is given by the following equation :

$$x(l) = x_1(l).f_1 + x_2(l).f_2$$

where

$$f_1 = \frac{2}{\pi} \tan^{-1} \left[\left(\frac{l}{L_t} \right)^p \right]$$

$$f_2 = \frac{2}{\pi} \tan^{-1} \left[\left(\frac{L_t}{l} \right)^p \right]$$

L_t = transition index

p = power

x = generic coordinate

l = index

The surface normal is determined by defining two body-tangent vectors at each surface grid point. The cross product of these two vectors divided by its length gives the unit normal, \mathbf{n} . From the unit normal, we can calculate a projection matrix, $\mathbf{P} = \mathbf{n}^T \mathbf{n} / \mathbf{n} \cdot \mathbf{n}$, which when post-multiplied by any vector would give the projection of that vector along

the unit normal. A cross-section of the grid shown in Fig. 2 illustrates the result of blending.

3.3 Zonal arrangement

The implementation of the flow solver requires multiple zones of a certain maximum size because of memory limitations. To accommodate this, the grid is divided into fourteen zones, half of which are shown in Fig. 3. No interpolation is required at the zonal interfaces. Symmetric zones are used to save on secondary storage because the metrics are identical for both sides of the symmetry plane.⁶ Note also that zones are separated circumferentially at the blowing slots for the implementation of the actuator plane as an inter-zonal boundary condition. The grid is 80x137x50 or 548000 points. For the generation of a grid of this size, the total Cray Y-MP CPU time required is 23 sec.

4. Numerical method

The flow is solved for using a version of the F3D code. F3D contains the algorithm developed by Steger et al.^{19,20} The implicit two-factor algorithm uses flux-vector splitting to upwind difference the convection terms in the streamwise direction, while retaining central differencing in the other directions. This scheme is unconditionally stable for the model wave equation and can have natural numerical dissipation and better stability properties than fully central difference algorithms.¹⁹

Due to the high Reynolds number flow in this study, the Baldwin-Lomax turbulence model,⁸ with modifications for cross-flow separation suggested by Degani and Schiff,⁹ is used. Values for y^+ are consistently less than 4 throughout the grid. The wake is assumed to be laminar. The flow on the wing is treated as fully turbulent.

The convergence rate is relatively slow because of the low Mach number used (0.2), the rounded leading-edge wing (which means that the primary separation line takes time to be established in a steady-state calculation), and due to high values of the grid transformation Jacobian in the stretched nose grid.

5. Actuator plane concept

The difference between using the actual geometry and using the actuator plane concept is shown in Fig. 4. Note that the actuator plane is, in effect, a discontinuity imposed as a boundary condition in the flow at an inter-zonal boundary. This concept has been used before on an ogive cylinder⁶ and the F-18 forebody.⁵ In the latter study, a comparison was made between resolving and not resolving the jet slot. The differences in results were found to be minimal for a delta wing test case.

The jet Mach number is calculated assuming incompressibility or jet exit pressure equal to that of freestream. The boundary condition at the jet interface of the zone below the jet is obtained by extrapolation from the interior points.

6. Results and Discussion

All cases were run at $M_\infty = 0.2$ and $Re = 1.2 \times 10^6$ based on the wing chord.

6.1 No blowing cases

6.1.1 $\alpha=30^\circ, \beta=0^\circ$

Figures 5, 6 and 7 show the stagnation pressure contours, simulated surface flow patterns and particle traces respectively for this case. Note that at this α the vortex stays unburst until it reaches the tail portion of the wing. This is evident from the sudden thickening of the core in both the particle traces and in the $C_{p_{stag}}$ contours. The primary and secondary vortices can also be seen on the $C_{p_{stag}}$ contours (Fig. 5). From Fig. 6, the primary separation line extends along the leading edge, and moves outboard. This variation in separation location is the main difference between this wing and sharp leading-edge wings where the primary separation line is fixed at the leading edge itself. The location of the primary separation line at the nose can be connected to a delay in the formation of the secondary line. An interesting feature to note is the formation of another vortex with rotation in the same sense as that of the primary one further downstream. Its development is then altered by the forced separation at the rectangular cross-section tail. Whether a whole series of vortices will be produced on an infinitely long wing is an intriguing possibility. A determining factor could be whether the primary leading-edge vortex feeding sheet stays attached to the primary separation line further downstream.

Figure 8 gives the calculated spanwise pressure coefficient distributions at five downstream stations. Here again the formation of the vortex is evident. A signature of a rounded leading-edge wing is clearly visible in the form of the wide leading-edge suction

peak. For sharp leading-edge wings this peak is often only a spike, thereby not contributing significantly to the lift.

6.1.2 $\alpha=50^\circ, \beta=0^\circ$

Figures 9, 10 and 11 show the stagnation pressure contours, simulated surface flow and particle traces for this case. At this α vortex breakdown is observed at 30% root-chord. The breakdown can be described as bubble type rather than spiral because of the fixed envelope which the streamlines and contours form and the extension of the secondary separation line downstream. Figure 10 shows that the primary separation line weakens further downstream because the flow at this α has a dominant cross-flow component. The surface flow patterns on the tail show a saddle point under the stagnated flow of the burst vortex. The vortex trajectory remains close to the wing due to the suction on the vortex and then follows the freestream direction in the wake.

Figure 12 gives the calculated pressure coefficient distributions at the same five downstream stations for this case. The footprint of a burst vortex in this case is a flattening of the suction pressure peak in the downstream locations. The leading-edge suction peak is also thinner than in the $\alpha=30^\circ$ case because of the more bluff body-type flow.

6.1.3 $\alpha=30^\circ, \beta=10^\circ$

To test the code and the blowing mechanism for initially asymmetric flows, and to get at least a crude approximation of a real-life maneuver, a number of cases are calculated for a wing in side-slip.

Figure 13 shows the particle traces from a preliminary computation. The most notable feature of this yawed case is the intensification of the breakdown on the windward side and the absence of breakdown on the leeward side. From the pressure coefficient distribution in Fig. 14 it can be seen that the windward side vortex is stronger as expected.

6.1.4 $\alpha=50^\circ, \beta=10^\circ$

Figure 15 gives a preliminary plot of the pressure distributions for this case. The same features of asymmetry noted above are again evident.

6.2 Blowing cases

The blowing momentum coefficient is defined by

$$C_\mu = \frac{m_j U_j}{\rho_\infty S_{ref}}$$

6.2.1 $\alpha = 30^\circ, \beta = 0^\circ$

A range of blowing coefficients was used to effectively show the influence of blowing on the aerodynamics. From the experiments, a value of C_μ of about 0.04 marks the boundary of the useful blowing region. Increasing the blowing intensity further produced no extra rolling moment at this pre-stall angle of attack. In order to try and capture this non-linear behaviour, a range of C_μ from 0 to 0.06 was chosen in increments of 0.01.

The effect of tangential leading-edge blowing on the flow at this α for three blowing coefficients is shown in the particle traces of Figs. 16, 17 and 18. The

blowing slot is indicated on the pilot's right with a thick line on the side of the wing. Note how an increase in blowing intensity effectively moves the leading-edge vortex inboard, until at some blowing coefficient the flow becomes completely attached. Note also, more importantly, that at this α , the flow on the unblown side remains essentially unchanged by the blowing, and is therefore uncoupled. At lower C_{μ} values, the leading-edge vortex on the blown side is not as focused or strong as on the unblown one, and breakdown seems to occur sooner.

Figures 19, 20 and 21 show the stagnation pressure contours for three values of C_{μ} . The contours show how the vortex is flattened compared to the unblown side until it is eventually 'blown away'.

Figures 22, 23 and 24 show the simulated surface flow contours. Here the effectiveness of blowing in moving the primary separation line is evident. Note that at the higher blowing coefficients the surface flow goes over the symmetry line, but does not significantly affect the unblown side flow.

The calculated spanwise pressure coefficients at one downstream station as a function of increased blowing intensity is shown in Fig. 25. The uncoupling is evident in the collapse of the curves on the unblown side. On the blown side, the re-attachment of the leading-edge vortex with increased blowing can be seen. The lift contribution of the leading-edge suction peak also increases with increased blowing. This will later be seen to contribute to a blown-side-up rolling moment.

6.3 Comparison with experiment

Before comparisons are made, it should be noted that the experiments were run at $M_\infty=0.058$, $Re=4 \times 10^5$ and $M_\infty=0.12$, $Re=8 \times 10^5$ for all α and β cases, and that significant wind tunnel wall interference at high α is noted⁴ due to a relatively small test section. It should be pointed out, however, that the aim of the experiment was to show the effect of blowing, and therefore the *difference* in coefficient values between the blown and unblown cases, rather than the absolute values of the coefficients. Reservations are also expressed⁴ as to the accuracy of the stall angle and burst locations in view of comparison with other similar experiments. To summarize, comparison studies between computation and experiment should only be made if the difference between blown and unblown coefficients are used. Before comparing specific quantities, it should be mentioned that an angle of attack correction is expected to be justified. Specifically, it is suspected that the effective angle of attack in the experiment is higher than the geometric angle of attack due to wall interference effects. This is being investigated carefully.

6.3.1 Comparison of pressure coefficients

The difference in pressure coefficients when blowing is applied is used as a measure of comparing with experiment. ΔC_p is defined as $-C_{p_unblown} - (-C_{p_blown})$. This means that a positive ΔC_p would correspond to a reduction in suction peak. Figures 26, 27 and 28 show how this measure changes with blowing coefficient for $\alpha = 30^\circ$. The reduction in the pressure peak agrees reasonably well with experiment. The only real discrepancy is at low C_μ where the experimental difference goes slightly negative. This implies that in the experiment the leading-edge vortex spread out and

moved inboard as its strength was reduced by the blowing.

6.3.2 Comparison of rolling moment coefficient

Figure 29 gives the rolling moment comparison for the $\alpha = 30^\circ$ case. Note how the saturation effect is captured as well as the saturation level. This confirms the notion in the experimental study⁴ that blowing for a pre-stall angle of attack is only useful in a limited range. Since the rolling moment is zero at zero blowing, the figure actually shows the difference in rolling moment coefficient between blowing and no blowing.

6.3.3 Comparison of normal force coefficient

The difference in normal force coefficients as blowing is applied is shown for the $\alpha = 30^\circ$ case in Fig. 30. The difference is calculated the same way as above for the pressure coefficient. The same trend is observed in the computations as in the experiment, but there is a distinct difference in the turning point where after a reduction in normal force with increased blowing, the normal force increases again. One explanation for this discrepancy could be that in the computations, the calculated flow is further from the stall point as in the experiment⁴, where it was determined to be at $\alpha = 40^\circ$. In other words, an angle of attack correction should be made as was mentioned earlier. The reason for this can be seen on the same plot where the $\alpha = 20^\circ$ normal force coefficient differences are shown. The turning point is at a lower C_{μ} value for this angle of attack further away from the stall point. Another supporting fact is that the absolute normal force

coefficients are much higher in the experiments at 30° than in the computations. More computations are being planned to determine the stall angle for the computational configuration. Unfortunately the computations are too expensive to allow for a whole range of angle of attacks needed to determine the computational stall point.

Finally, a comparison is made for the absolute normal force coefficient values. Figure 31 shows the computational C_L values for the $\alpha=30^\circ, \beta=0^\circ$ and $\alpha=50^\circ, \beta=0^\circ$ cases as compared to the Leading-Edge Suction Analogy theory of Polhamus²¹ for incompressible flow and experiments^{16,22,23,24} for sharp leading-edge wings at comparable AR. The tail on the wing under study gives it an effective $AR=1.224$. The Polhamus analogy is for sharp leading-edge and pure delta wings and is therefore only useful in quantitative comparisons. The theory is also only expected to be accurate for α 's before breakdown occurs.²¹ Unfortunately, only normal force coefficients and no lift or drag coefficients were measured in the experiments,^{3,4} so a direct comparison of lift is not possible.

Soltani et al²² showed that an increase in Reynolds number decreases the vortex lift at a given α . This could partly explain why the normal force coefficient values of the computations are below that of experiment.

6.3.4 Comparison of pitching moment coefficient

Here, we see essentially the same trend as for the normal force coefficient difference, as is shown in Fig. 32. The same arguments also hold.

7. Future work

Grid resolution is another key factor in accurately capturing leading-edge vortices. In order to determine whether the lack of good agreement with experiment is due to experimental conditions (e.g. wind tunnel wall interference or lower freestream velocity) or due to numerical inaccuracy due to grid coarseness, a finer grid has been generated. The points are more concentrated in the vortex trajectory area. Computations with this configuration are being planned.

Recent experimental results with a similar wing²⁵ at the University of Bath has shed some light on the poor comparison of absolute values obtained above. Fig.33 shows a comparison of the rolling moment coefficient contours in α - C_{μ} space for the Stanford and Bath experiments. The planform of the wings are identical, but the thicknesses are 6% and 3.3% respectively. The blowing slots are different also, but most importantly, wind tunnel wall interference is much less for the Bath experiments with a wing/tunnel area ratio of only 5% at $\alpha = 90^\circ$. The contours show the same basic control reversal, but for the Bath case it is confined to the stall angles of attack. For instance at $\alpha = 50^\circ$ control reversal occurred in the Stanford experiments, but not in the Bath experiments. Preliminary computational results at 50° also show no control reversal. Another point from Ref.25 is the values of C_N obtained. In the Stanford experiments⁴, the value at $\alpha = 30^\circ$ was about 1.8, whereas for the Bath experiments it was about 1.4, another indication of the influence of wind tunnel walls. In the computations, the value is about 1.2. Computations at $\alpha = 40^\circ$ are now being run to try to determine the stall angle and whether control reversal is obtained.

Comparison with other Navier-Stokes codes such as TNS²⁶⁻²⁹ and different turbulence models are also being planned.

8. Conclusions

This report shows that a successful calculation of the complicated flowfield around a rounded leading-edge delta wing at angles of attack and yaw with and without tangential leading-edge blowing is possible with current resources. The results obtained thus far compare reasonably well with experiments if the difference in coefficients between unblown and blown cases is used. The effectiveness of blowing as a means to provide roll control at post-stall angles of attack is illustrated. Future work will extend the envelope of cases in order to fully validate the computational results with experiments.

9. Acknowledgements

The author wishes to thank Leonard Roberts, Eugene Tu and Domingo Tavella for their support. The author also wishes to thank the Fixed Wing Aerodynamics Branch at NASA Ames Research Center for their support and the use of their facilities.

References

1. Wood, N.J. and Roberts, L., Control of Vortical Lift on Delta Wings by Tangential Leading-Edge Blowing, *J.Aircraft*, Vol.25 No.3, pp.236-243, March 1988.
2. Yeh, D., Tavella, D., Roberts, L. and Fujii, K., Numerical Study of the Effect of Tangential Leading-Edge Blowing on Delta Wing Vortical Flow, AIAA 89-0341, 27th Aerospace Sciences Meeting, Jan. 1989, Reno, NV.
3. Celik, Z.Z., Roberts, L. and Wood, N.J., An Investigation of Asymmetric Vortical Flows over Delta Wings with Tangential Leading-Edge Blowing at High Angles of Attack, AIAA 90-0103, 28th Aerospace Sciences Meeting, 8-11 Jan. 1990, Reno, NV.
4. Wood, N.J., Roberts, L. and Zelik, Z., Control of Asymmetric Vortical Flows over Delta Wings at High Angles of Attack, *J.Aircraft* Vol.27 No.5, pp.429-435, May 1990.
5. Tavella, D.A., Schiff, L.B. and Cummings, R.M., Pneumatic Vortical Flow Control at High Angles of Attack, AIAA 90-0098, 28th Aerospace Sciences Meeting, 8-11 Jan. 1990, Reno, NV.
6. Font, G. and Tavella, D., High Alpha Aerodynamic Control by Tangential Fuselage Blowing, AIAA 91-0620, 29th Aerospace Sciences Meeting, 7-10 Jan. 1991, Reno, NV.
7. Ekaterinaris, J.A. and Schiff, L.B., Vortical Flows over Delta Wings and Numerical Prediction of Vortex Breakdown, AIAA 90-0102, 28th Aerospace Sciences Meeting, 8-11 Jan. 1990, Reno, NV.
8. Baldwin, B.S. and Lomax, H., Thin Layer Approximation and Algebraic Model for Separated Turbulent Flows, AIAA 78-0257, Jan. 1978.
9. Degani, D. and Schiff, L.B., Computation of Turbulent Supersonic Flows Around Pointed Bodies Having Crossflow Separation, *J. Comp. Phys.*, Vol.66, pp.173-196, 1986.
10. Smith, J.H.B., Improved Calculation of Leading Edge Separation from Slender Thin Delta Wings, *Proc. Roy. Soc. A*, Vol.306, pp.67-99, 1968.
11. Kandil, O.A. and Chuang, H.A., Unsteady Navier-Stokes Computations Past Oscillating Delta Wing at High Incidence, AIAA 89-0081, 27th Aerospace Sciences Meeting, 9-12 Jan. 1989, Reno, NV.
12. DeJarnette, F.R. and Shawn, H.W., Numerical Determination of Secondary Separation on Delta Wings in Subsonic Flow, *J.Aircraft*, Vol.22 No.7, pp.602-608, July 1985.
13. Hsu, C.-H. and Hartwich, P.-M., Computation of Vortical Interaction for a Sharp-Edged Double-Delta Wing, *J.Aircraft*, Vol.25 No.5, pp.442-447, May 1988.
14. Krist, S.L., Thomas, J.L., Sellers, W.L. and Kjelgaard, S.O., An Embedded Grid Formulation Applied to a Delta

- Wing AIAA 90-0429, 28th Aerospace Sciences Meeting, Jan. 8-11, 1990, Reno, NV.
15. Gordnier, R.E and Visbal, M.R., Unsteady Navier-Stokes Solutions for a Low Aspect Ratio Delta Wing, AIAA 90-1538, 21st Fluid Dynamics, Plasma Dynamics and Lasers Conference, June 18-20, 1990, Seattle, WA.
 16. Deese, J.E., Agarwal, R.K. and Johnson, J.G., Calculation of Vortex Flowfields Around Forebodies and Delta Wings, AIAA 90-0176, 29th Aerospace Sciences Meeting, Jan. 7-10, 1991, Reno, NV.
 17. Vinokur, M., On One-Dimensional Stretching Functions for Finite-Difference Calculations, J.Comp.Phys., Vol. 50, pp.215-234, 1983.
 18. Tavella, D.A., Private communication.
 19. Steger, J.L., Ying, S.X. and Schiff, L.B., A Partially Flux-Split Algorithm for Numerical Simulation of Unsteady Viscous Flows, Proc. of Workshop on CFD, UC Davis, 1986.
 20. Ying, S.X., Steger, J.L., Schiff, L.B. and Baganoff, D., Numerical Simulation of Unsteady, Viscous High Angle of Attack Flows Using a Partially Flux-Split Algorithm, AIAA 86-2179, 1986.
 21. Polhamus, E.C., Prediction of Vortex-Lift Characteristics by a Leading-Edge Suction Analogy, J.Aircraft, Vol.8 No.4, April 1971, pp.193-199.
 22. Soltani, M.R., Bragg, M.B. and Brandon, J.M., Measurements on an Oscillating 70-Deg Delta Wing in Subsonic Flow, J.Aircraft, Vol.27 No.3, March 1990, pp.211-217.
 23. Wentz, W.H., Wind Tunnel Investigations of Vortex Breakdown on Slender Sharp-Edged Wings, Ph.D. Dissertation, University of Kansas, Lawrence, KS, 1968.
 24. Hummel, D. and Srinivasan, P.S., Vortex Breakdown Effects on the Low-Speed Characteristics of Slender Delta Wings in Symmetrical Flow, J.Royal Aeronautical Soc., Vol.71, April 1967, pp.319-322.
 25. Greenwell, D.I. and Wood, N.J., Control of Asymmetric Vortical Flows, AIAA 91-3272-CP, AIAA 9th Applied Aerodynamics Meeting, Sept. 23-25, 1991, Baltimore, MD.
 26. Holst., T.L., Kaynak, U., Gundy, K.L., Thomas, S.D. and Flores, J., Numerical Solution of Transonic Wing Flows Using an Euler/Navier-Stokes Zonal Approach, J. Aircraft, Vol.24 No.1, January 1987, pp.17-24.
 27. Flores, J., Convergence Acceleration for a Three-Dimensional Euler/Navier-Stokes Zonal Approach, AIAA Journal, Vol.24 No.9, September 1986, pp.1441-1442.
 28. Kaynak, U., Holst, T.L. and Cantwell, B.J., Computation of Transonic Separated Wing Flows Using an Euler/Navier-Stokes Zonal Approach, NASA TM 88311, July 1986.
 29. Tu, E.L., Navier-Stokes Simulation of a Close-Coupled Canard-Wing-Body Configuration, AIAA 91-0070, 29th Aerospace Sciences Meeting, Jan. 7-10, 1991, Reno, NV.

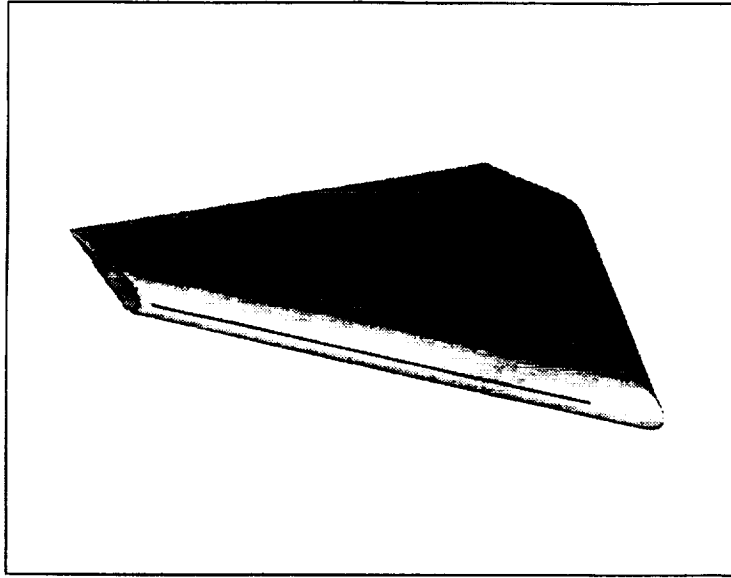


Fig.1 Perspective view of wing with blowing slot

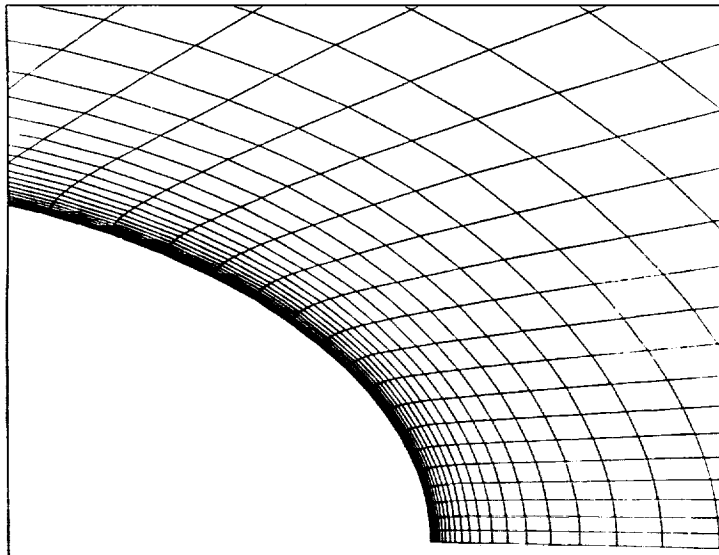


Fig.2 Close-up of nose grid showing effect of blending

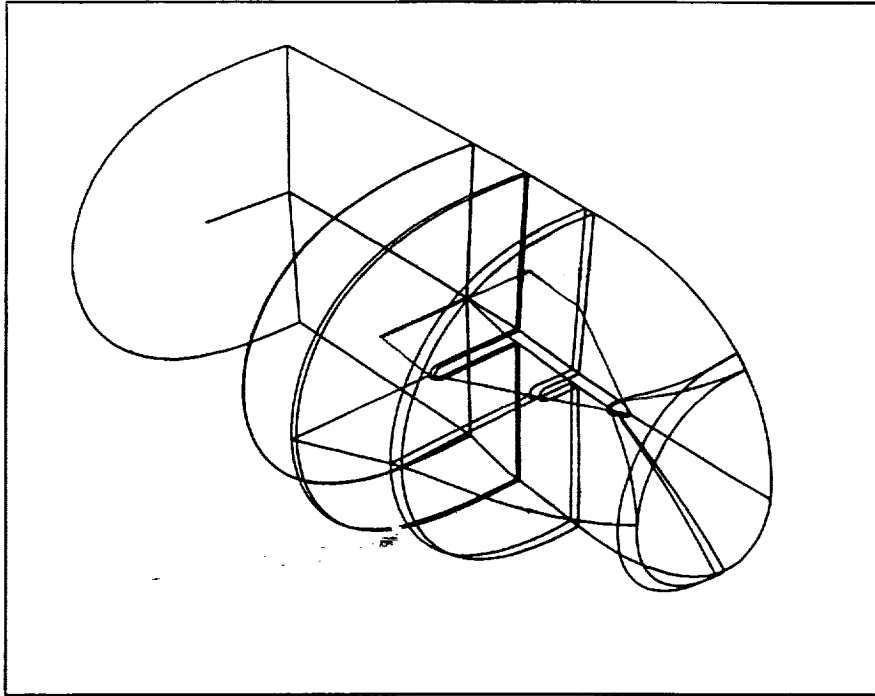


Fig.3 Zonal arrangement of grid

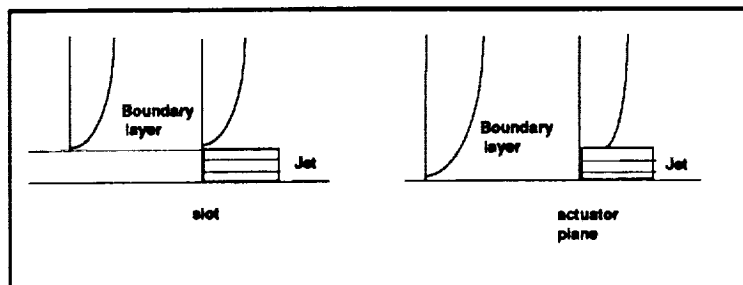


Fig.4 Actuator plane concept (Ref. 5)

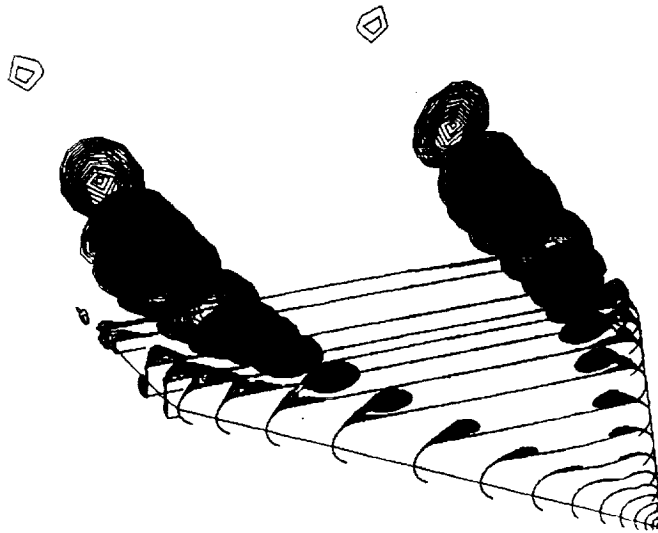


Fig.5 Stagnation pressure contours ($\alpha=30^\circ, \beta=0^\circ$)

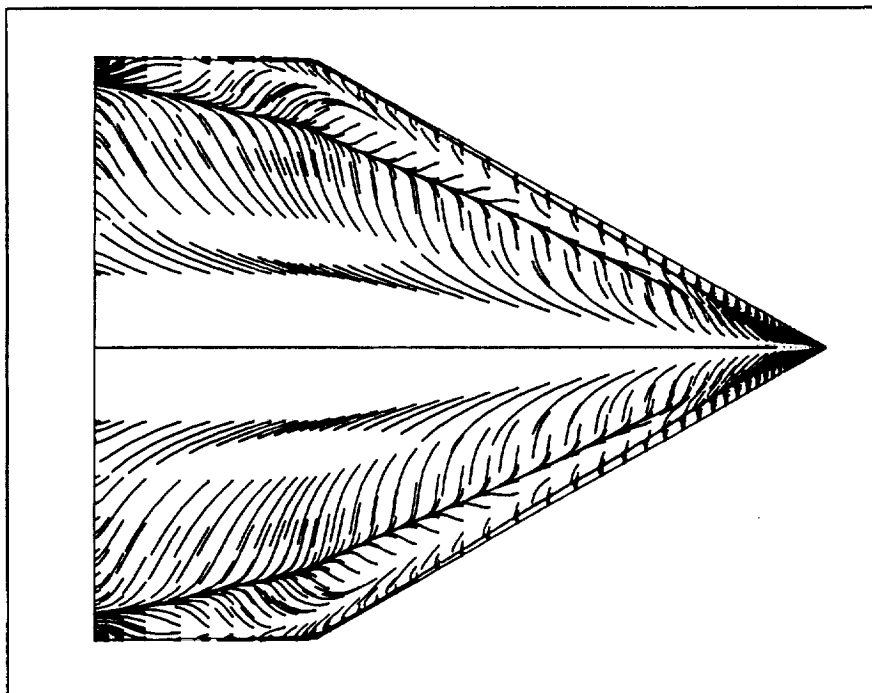


Fig.6 Computed surface flow patterns ($\alpha=30^\circ, \beta=0^\circ$)

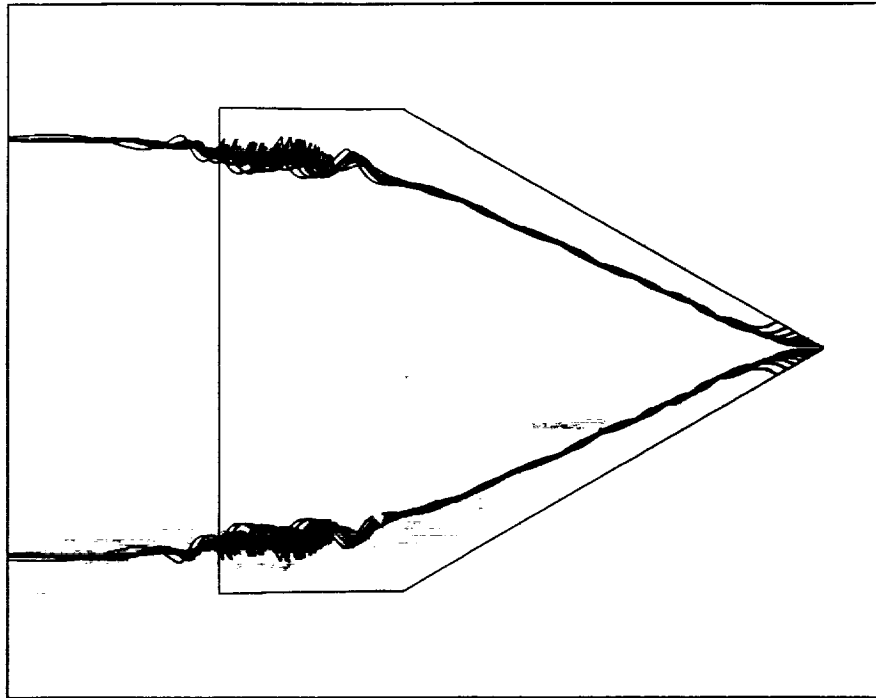


Fig.7 Particle traces ($\alpha=30^\circ, \beta=0^\circ$)

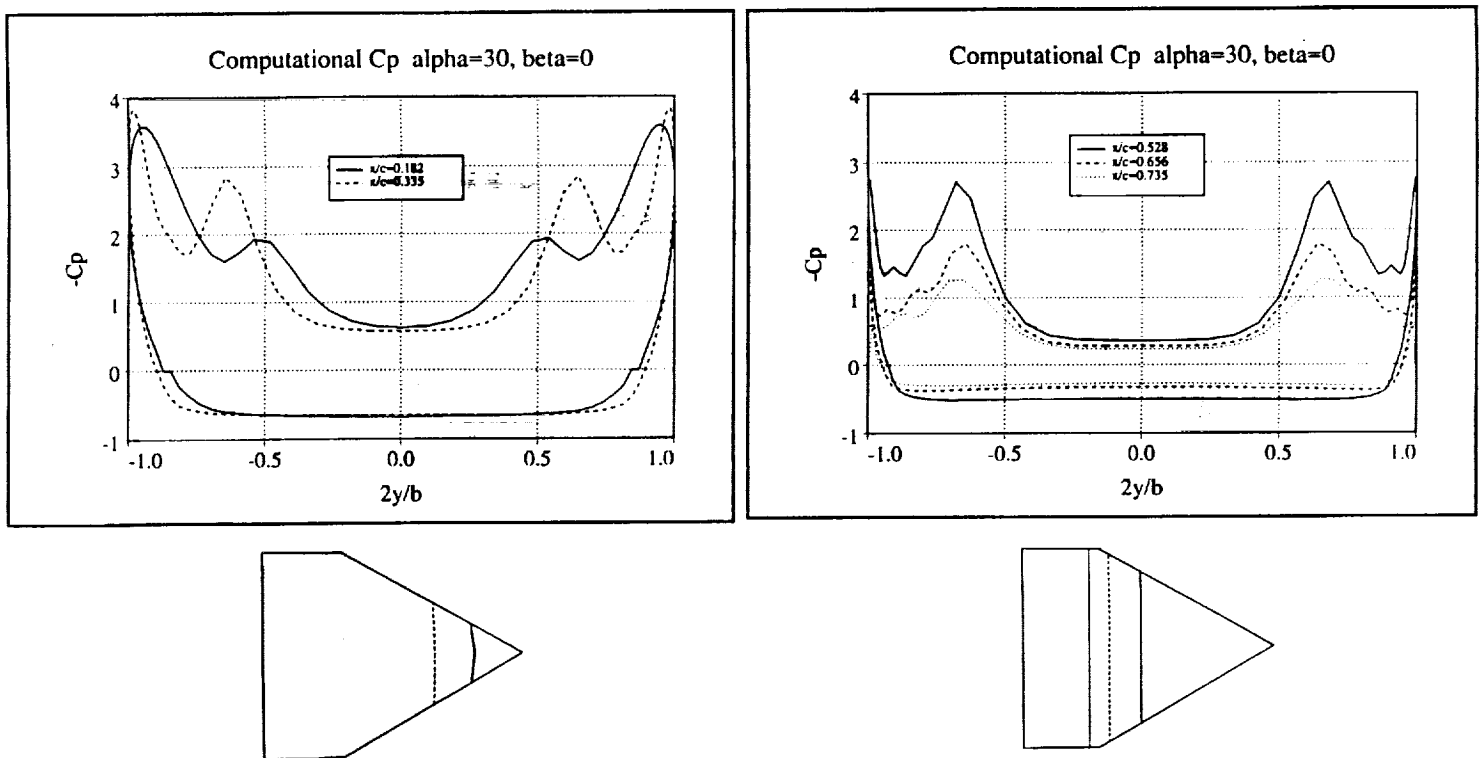


Fig.8 Pressure coefficient distributions ($\alpha=30^\circ, \beta=0^\circ$)

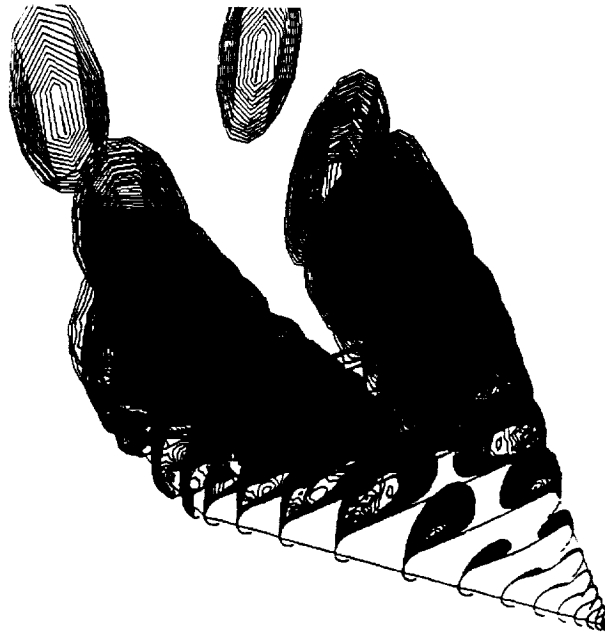


Fig.9 Stagnation pressure contours ($\alpha=50^\circ, \beta=0^\circ$)

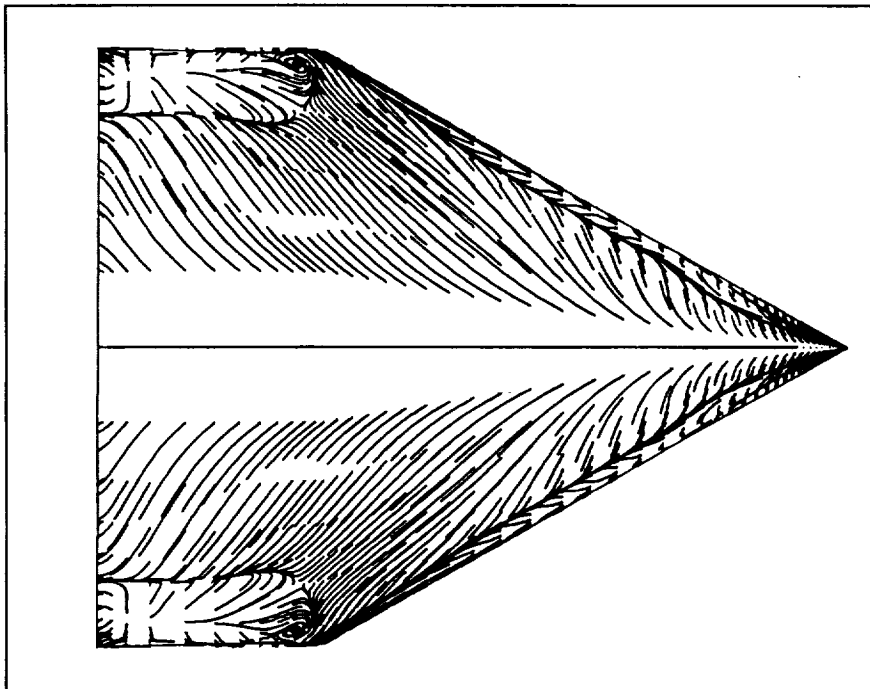
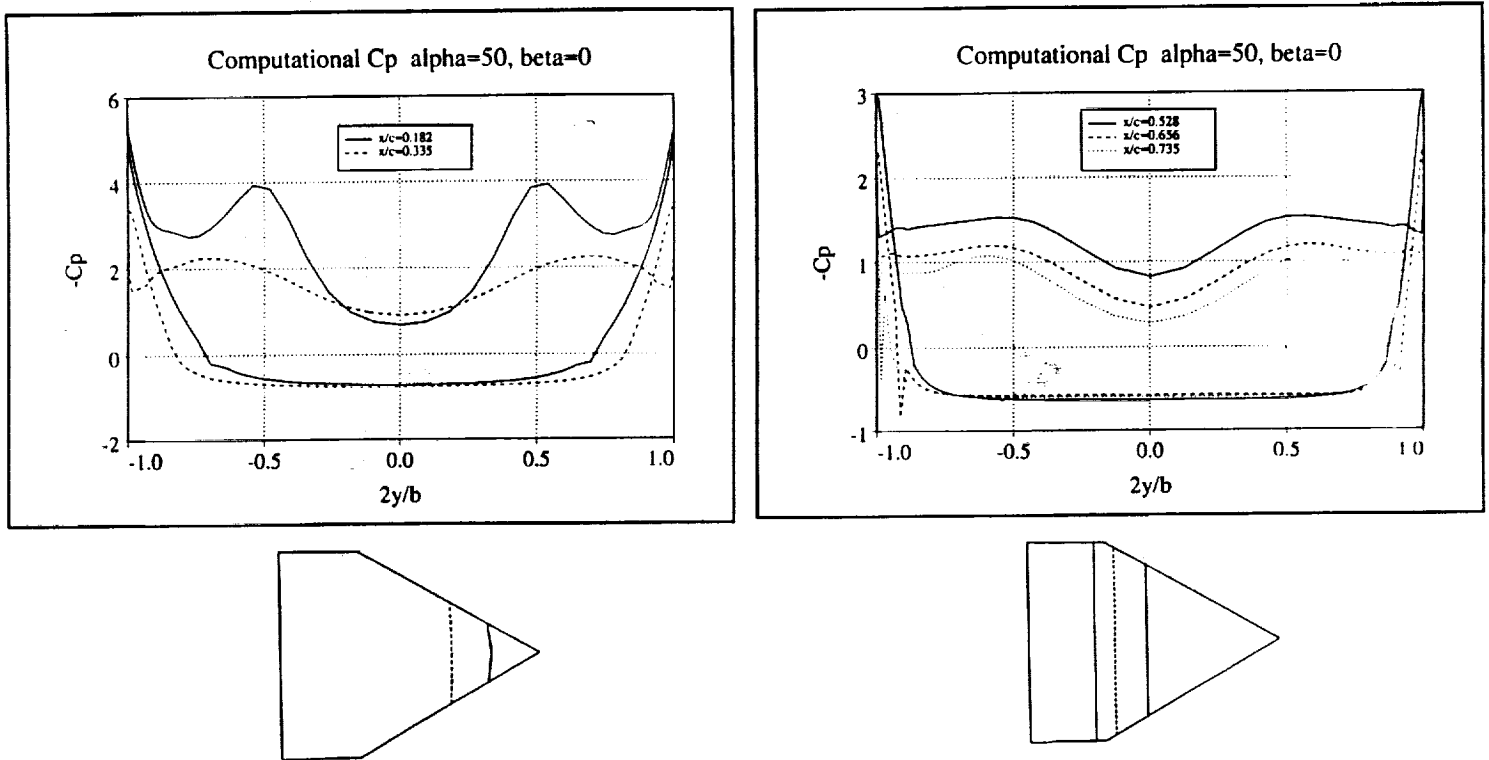


Fig.10 Computed surface flow patterns ($\alpha=50^\circ, \beta=0^\circ$)



Fig.11 Particle traces ($\alpha=50^\circ, \beta=0^\circ$)



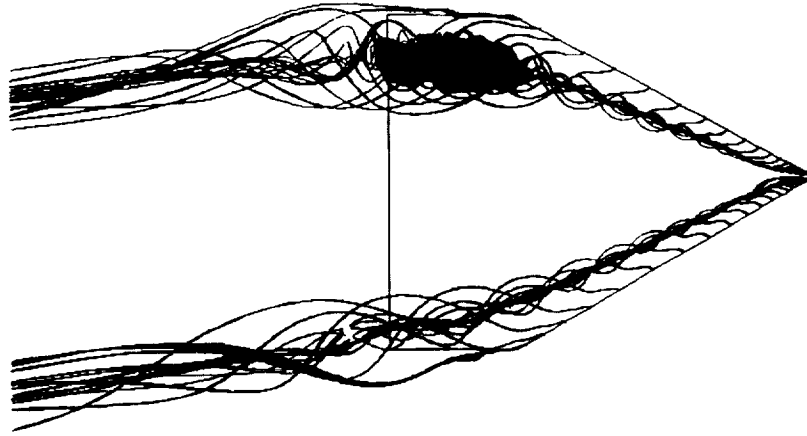


Fig.13 Particle traces ($\alpha=30^\circ, \beta=10^\circ$)

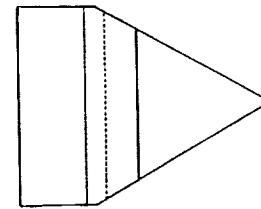
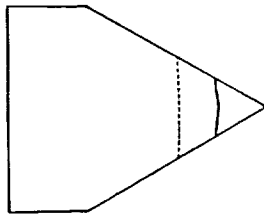
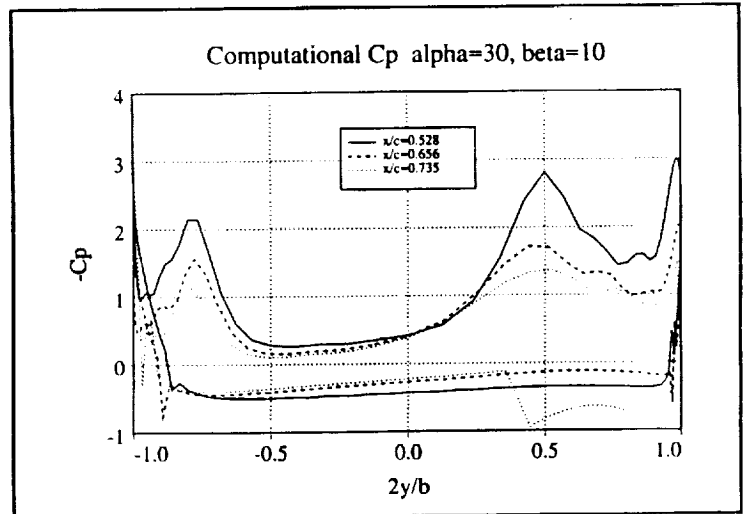
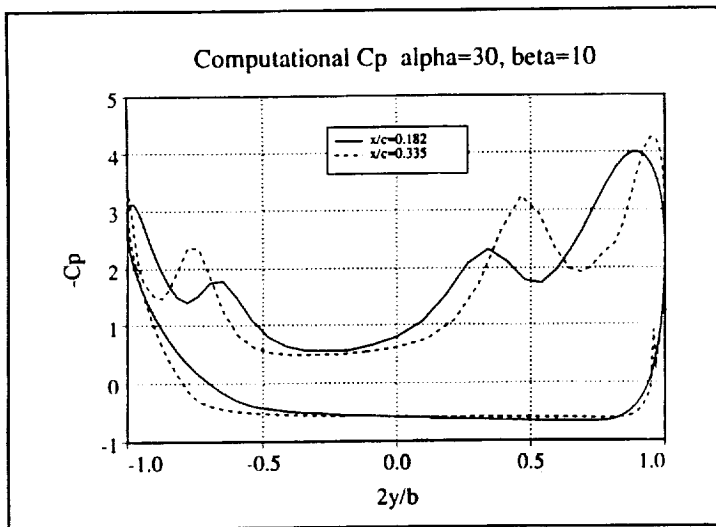


Fig.14 Pressure coefficient distributions ($\alpha=30^\circ, \beta=10^\circ$)

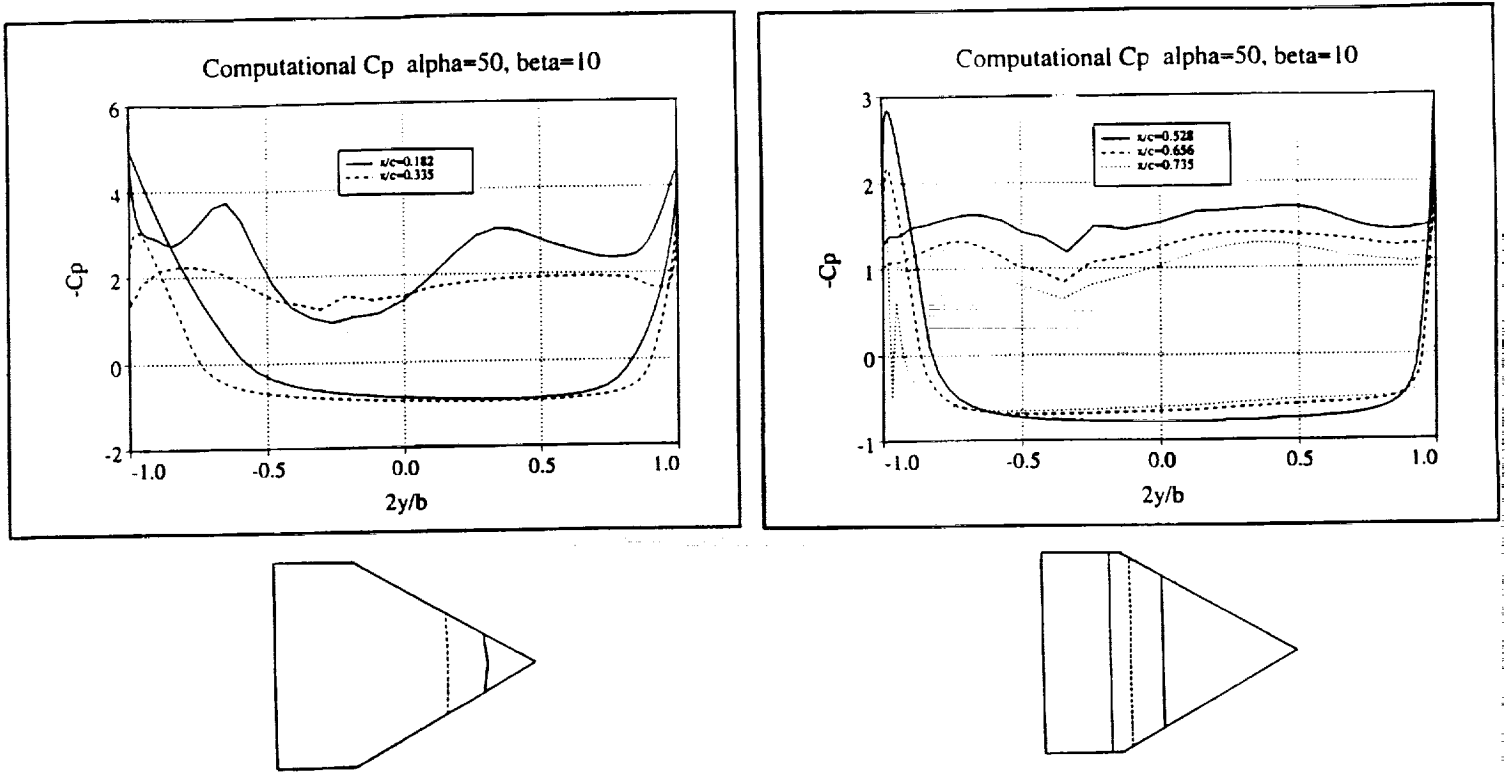


Fig.15 Pressure coefficient distributions ($\alpha=50^\circ, \beta=10^\circ$)

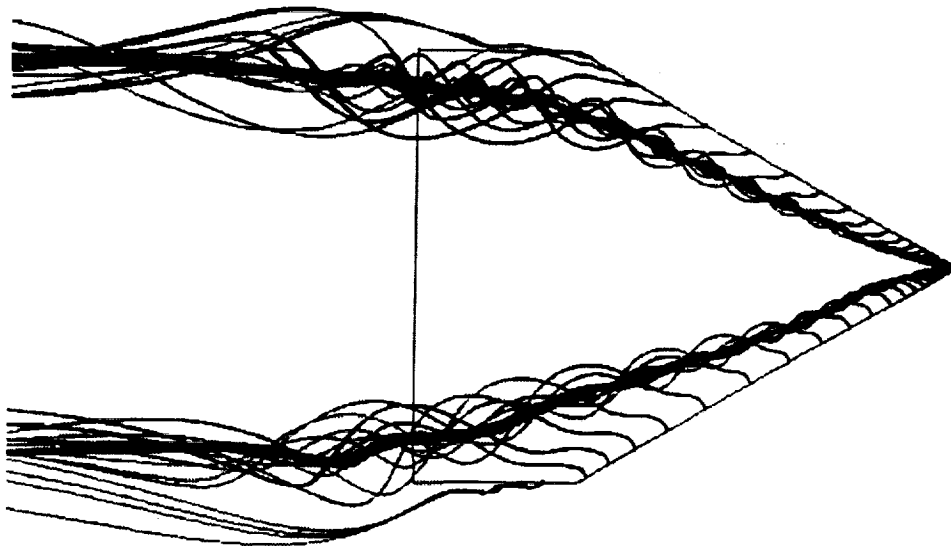


Fig.16 Particle traces ($\alpha=30^\circ, \beta=0^\circ, C_\mu=0.01$)

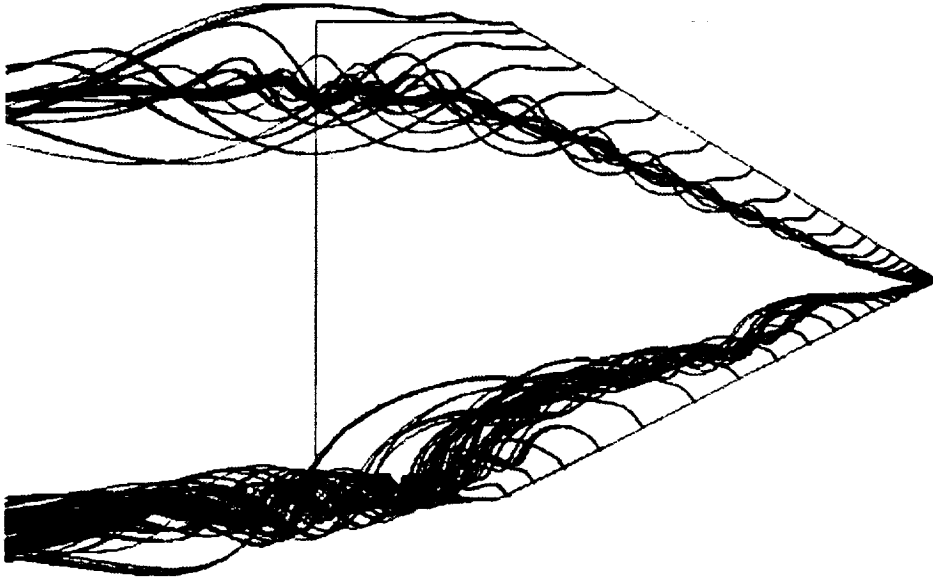


Fig.17 Particle traces ($\alpha=30^\circ, \beta=0^\circ, C_\mu=0.02$)

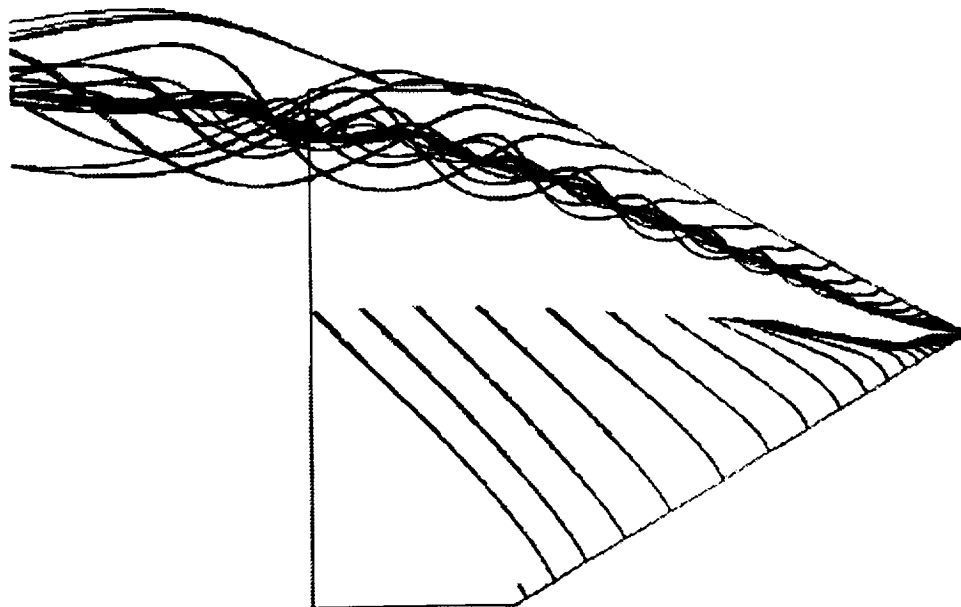


Fig.18 Particle traces ($\alpha=30^\circ, \beta=0^\circ, C_\mu=0.03$)

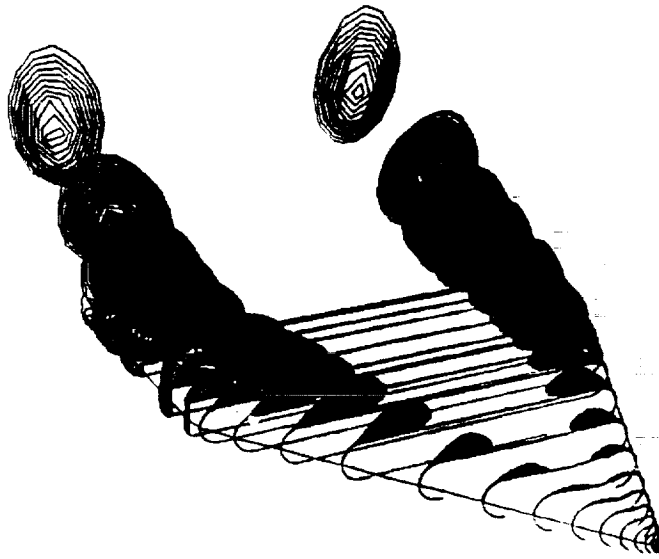


Fig.19 Stagnation pressure contours ($\alpha=30^\circ, \beta=0^\circ, C_\mu=0.01$)

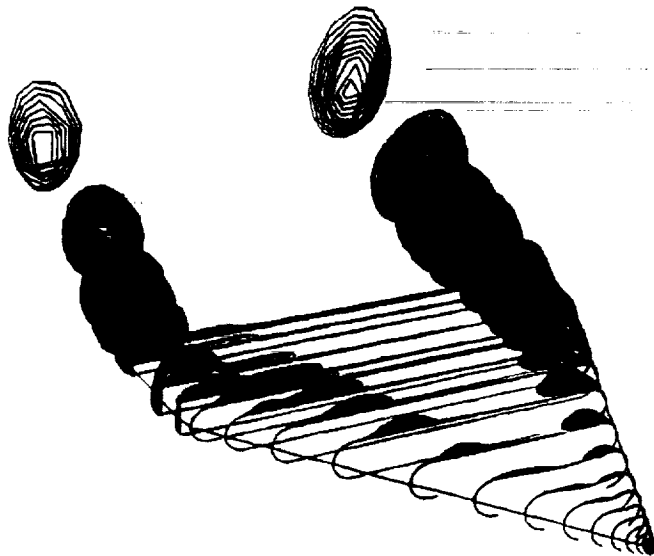


Fig.20 Stagnation pressure contours ($\alpha=30^\circ, \beta=0^\circ, C_\mu=0.02$)

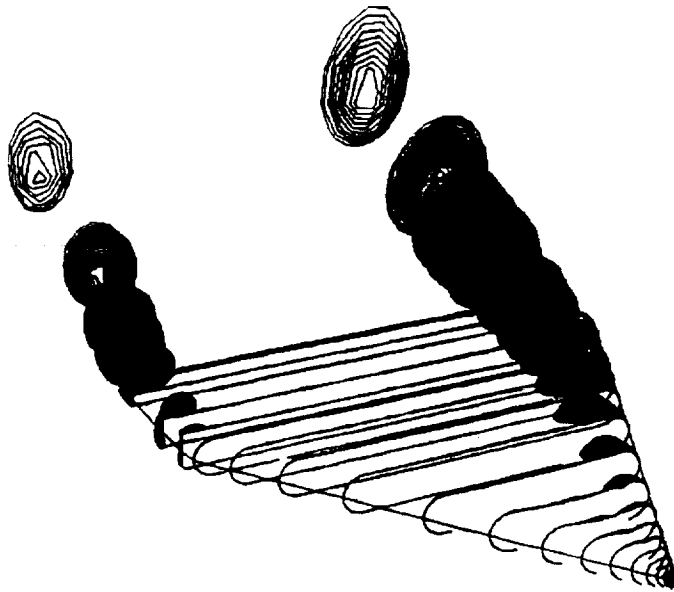


Fig.21 Stagnation pressure contours ($\alpha=30^\circ, \beta=0^\circ, C_\mu=0.03$)

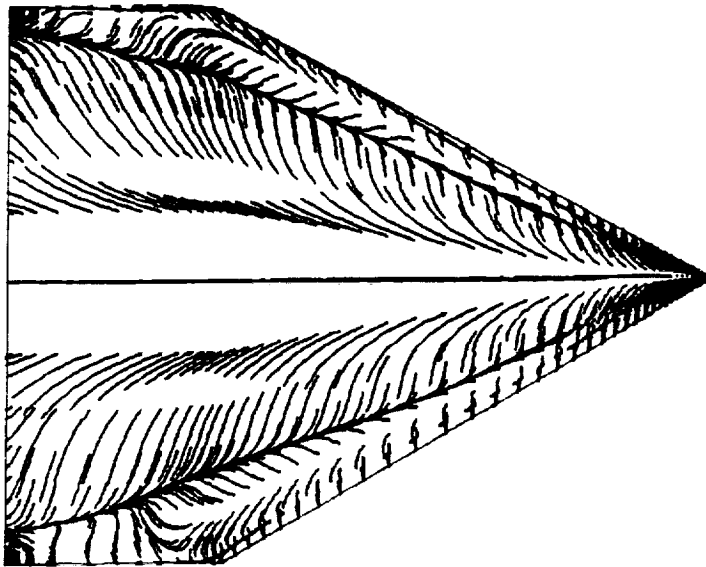


Fig.22 Computed surface flow patterns ($\alpha=30^\circ, \beta=0^\circ, C_\mu=0.01$)

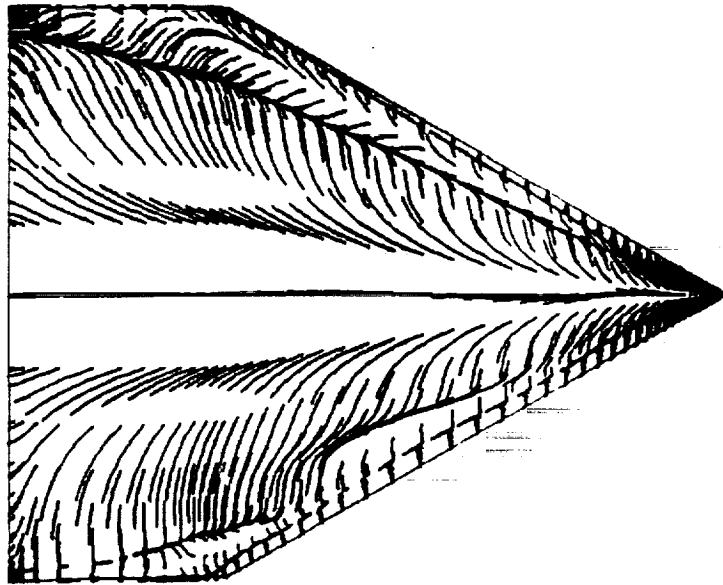


Fig.23 Computed surface flow patterns ($\alpha=30^\circ, \beta=0^\circ, C_\mu=0.02$)

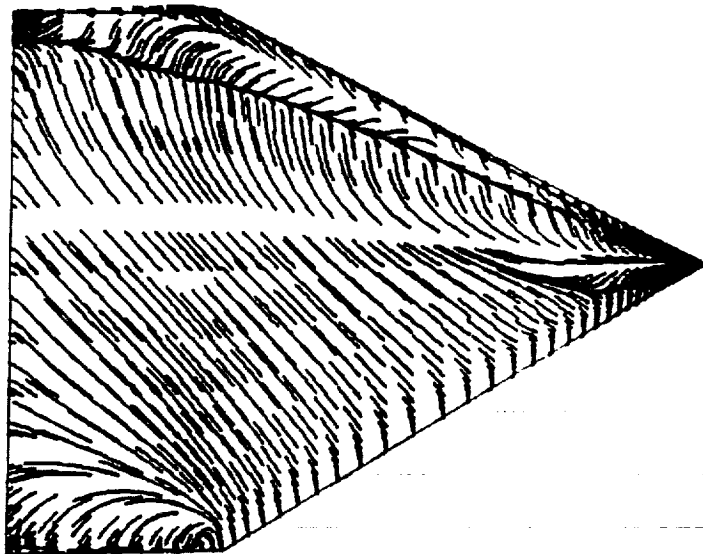


Fig.24 Computed surface flow patterns ($\alpha=30^\circ, \beta=0^\circ, C_\mu=0.03$)

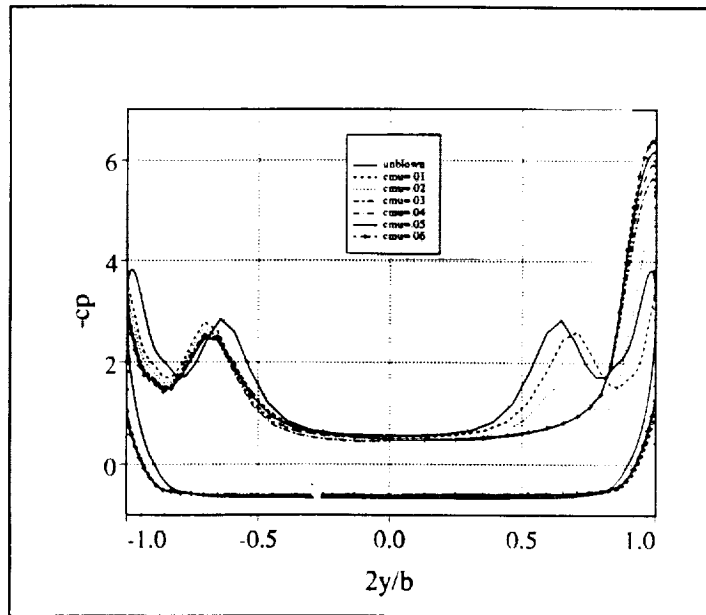


Fig.25 Spanwise pressure coefficient as function of blowing at one downstream station ($\alpha=30^\circ, \beta=0^\circ$)

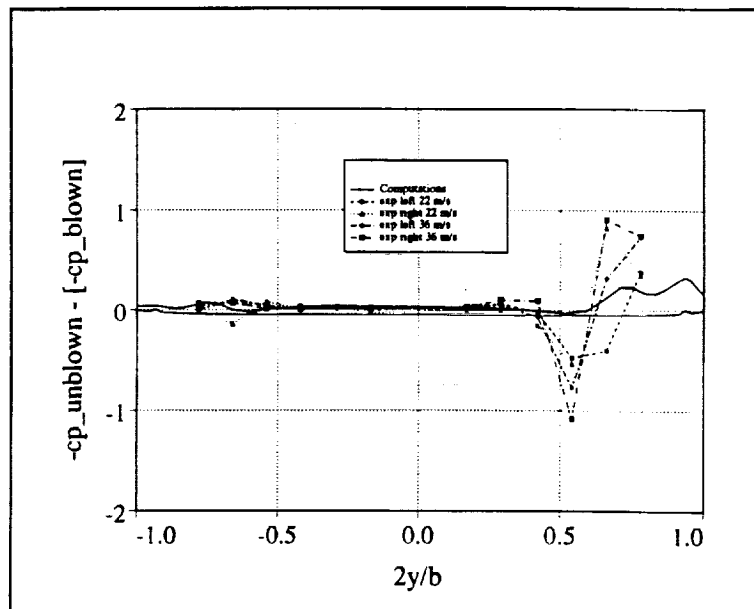


Fig.26 Comparison of change in pressure coefficient due to blowing between computation and experiment ($\alpha=30^\circ, \beta=0^\circ, C_\mu=0.01$)

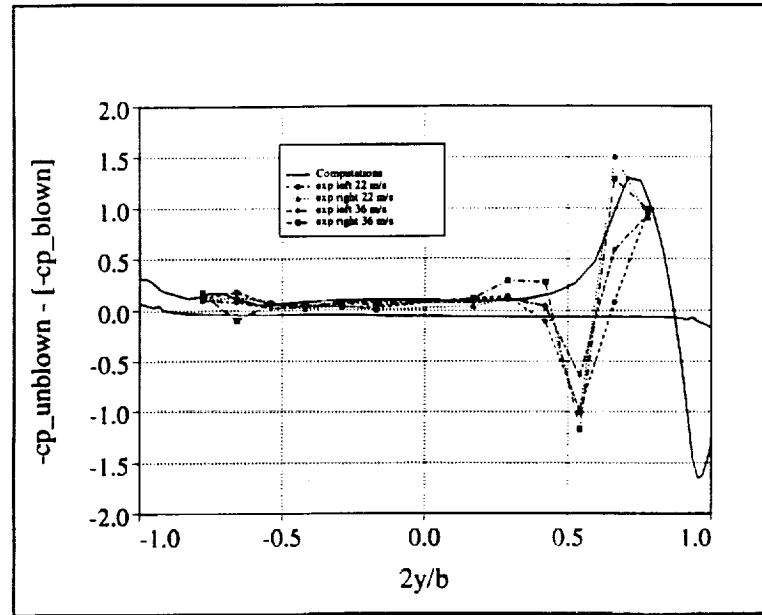


Fig.27 Comparison of change in pressure coefficient due to blowing between computation and experiment ($\alpha=30^\circ, \beta=0^\circ, C\mu=0.02$)

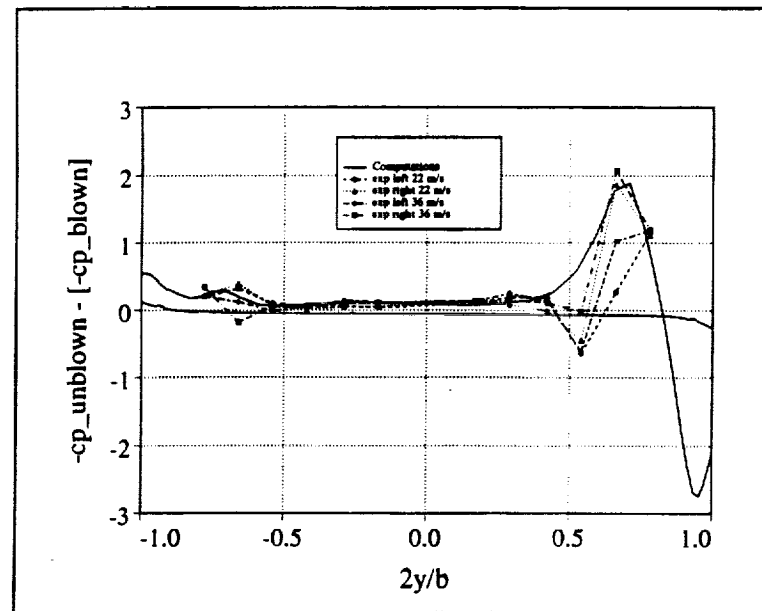


Fig.28 Comparison of change in pressure coefficient due to blowing between computation and experiment ($\alpha=30^\circ, \beta=0^\circ, C\mu=0.03$)

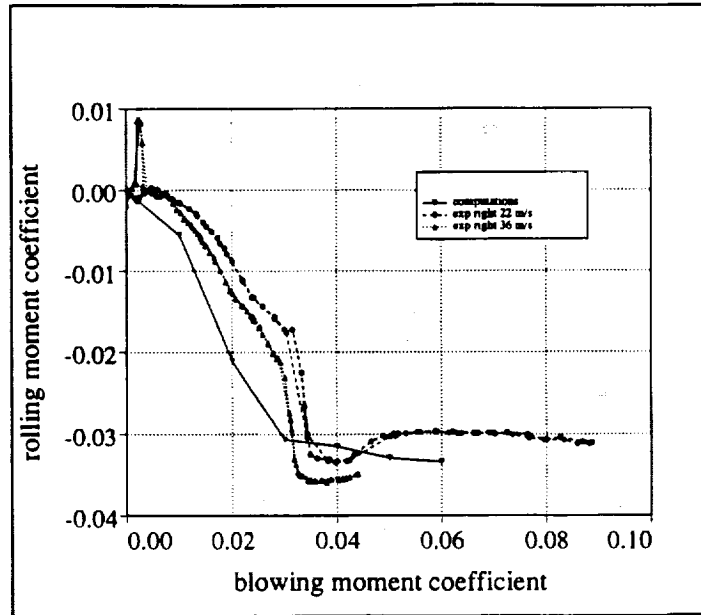


Fig.29 Comparison of rolling moment coefficient as a function of blowing moment coefficient between computations and experiment ($\alpha=30^\circ, \beta=0^\circ$)

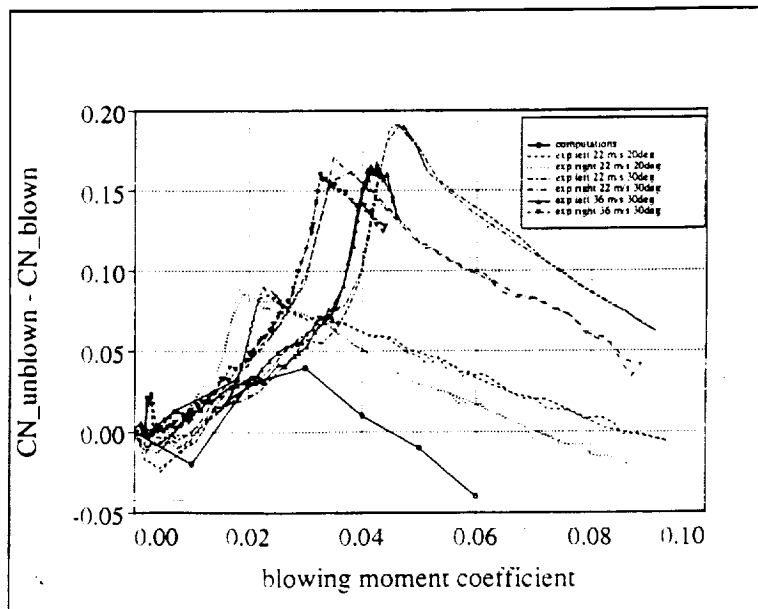


Fig.30 Comparison of change in normal force coefficient between computations and experiment ($\alpha=30^\circ, \beta=0^\circ$)

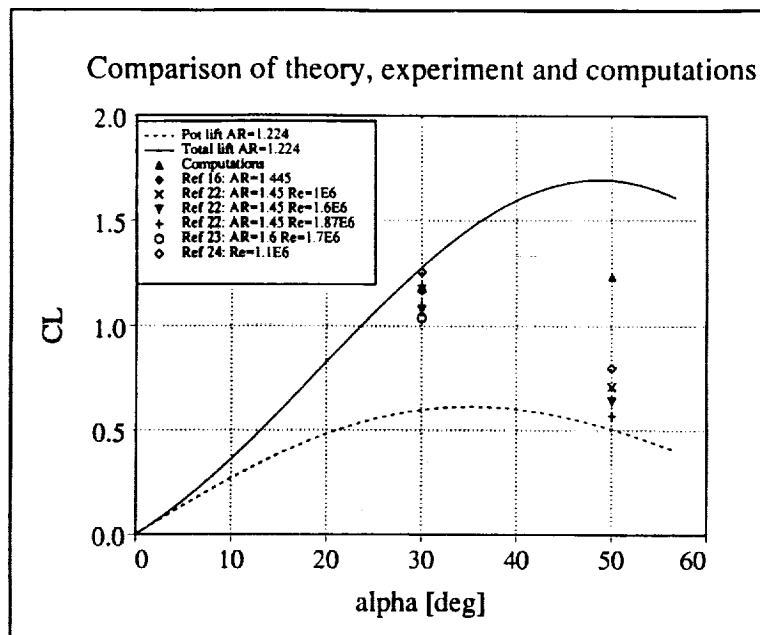


Fig.31 Comparison of ($\alpha=30^\circ, \beta=0^\circ$) and ($\alpha=50^\circ, \beta=0^\circ$) lift coefficient with Polhamus theory²¹ and experiment

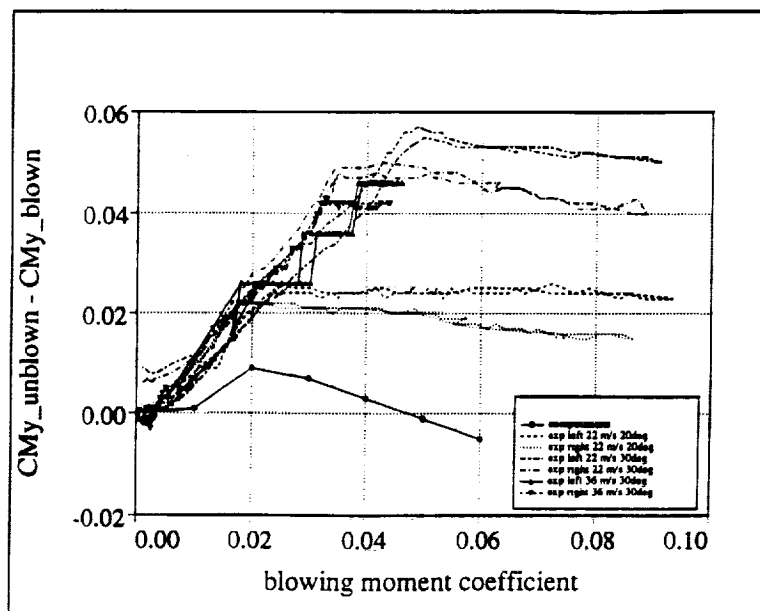


Fig.32 Comparison of change in pitching moment coefficient between computations and experiment ($\alpha=30^\circ, \beta=0^\circ$)

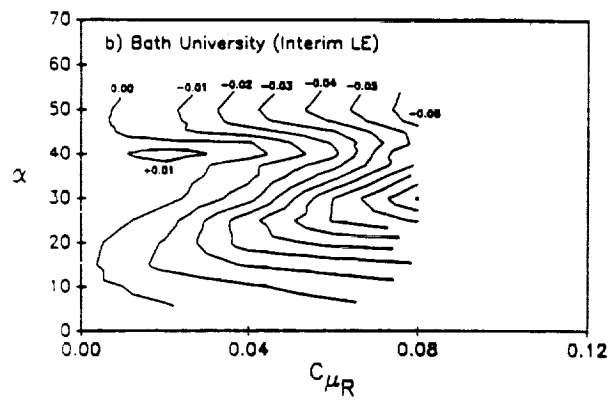
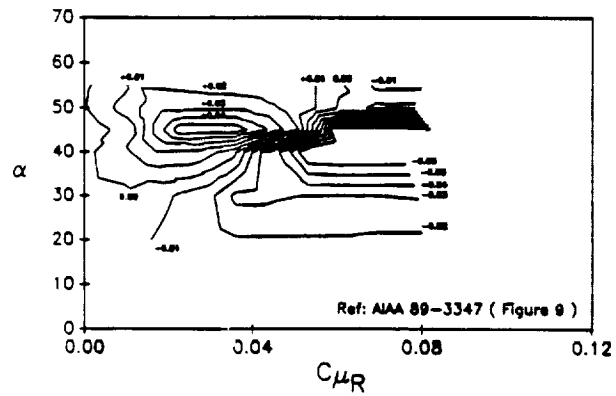


Fig.33 Comparison of rolling moment coefficient contours in α - C_{μ} space between Stanford^{3,4} and Bath²⁵ experiments

PAGE _____ INTENTIONALLY BLANK